Contact-free detection and visualization of guided waves in composites using an optical microphone

Caspar Wasle[*], Florian Heilemann[**], Björn Wohltmann, Rebecca Rodeck, Gerko Wende
German Aerospace Center (DLR), Hein-Saß-Weg 22, 21129 Hamburg

ABSTRACT

With increasing adoption of carbon fiber reinforced polymers in modern aircraft, new challenges in the maintenance of these structures arise. These materials are prone to internal damages such as delaminations, necessitating advanced non-destructive testing methods like ultrasonic testing. Guided ultrasound waves are a promising solution for testing large thin-walled structures like aircraft fuselages due to their long propagation range and high sensitivity to internal damage. However, traditional methods like laser-doppler vibrometry, while effective, are limited by their reliance on surface reflective properties, restricting their applicability in real-world maintenance scenarios. In this paper, a laser-based optical microphone is used to detect and visualize guided waves in carbon fiber reinforced polymer materials, featuring a very high bandwidth and independence from surface reflectivity. A robot test setup is developed to sample areas on the plate through repeated experiments. Signal processing enables the analysis of the wavefield and the visualization as two-dimensional wavefield images. By introducing defects into the plate, it is shown that these can be detected by changes in wave propagation patterns. With the flexible test setup using a robotic arm, the scalability of this approach to more complex structures with curvatures is demonstrated, highlighting its relevance for future use in aircraft maintenance.

Keywords: Contactless ultrasound, Optical microphone, Guided waves, Lamb waves, Maintenance, Robotics

1. INTRODUCTION

The use of Carbon Fiber Reinforced Polymers (CFRPs) in the aerospace industry has seen a remarkable increase over the past few decades. For instance, the usage of CFRPs in airframe and primary structures of commercial aircraft from Airbus and Boeing has increased from about 10% in 1990 to about 50% in 2015 in long-range models [1]. These composite materials are used due to their good performance in strength-to-weight ratio and design flexibility, making aircraft lighter and enabling higher fuel efficiency. Studies show that the usage of CFRPs in commercial aircraft has a technical CO_2 emission reduction potential of 20-25% [2]. For this reason, it is anticipated that future, more sustainable, aircraft generations will consist in large parts of composite materials. However, in contrast to traditional metal materials like aluminium, CFRPs have different damage mechanisms and therefore produce different damage patterns. In metal materials, a predominant failure mechanism is crack propagation due to stress concentration, where cracks initiate from the material surface. Composite materials, in contrast, are prone to delamination and matrix cracking, which are usually internal and harder to detect using traditional methods. The widespread use of composite materials therefore necessitates more advanced inspection methods capable of detecting internal defects [3].

With its ability to image the internal structure of carbon fiber composites at a reasonable cost, ultrasonic testing has become the procedure of primary choice for nondestructive testing in many applications [4]. Various techniques of ultrasonic testing exist, utilizing different ultrasound wave types and physical properties of these waves. Typically, an ultrasonic test setup consists of an excitation source for generating ultrasound waves in the structure and a receiver for detecting the resulting waves. A coupling medium such as water or gel is normally required to facilitate efficient and predictable transmission of ultrasound into the test material and to the receiver [5]. This approach, however, comes with its downsides as it is very hard to automate without submerging the test material in coupling fluid, especially for complex curved structural components [6]. Contactless ultrasonic testing is an emerging field in ultrasonic testing, promising a higher degree of flexibility and automation by eliminating the need for a coupling medium.

[*] ORCID: 0009-0003-7198-9186; caspar.wasle@dlr.de;
[**] ORCID: 0000-0003-0420-4505

Contactless ultrasonics

In most ultrasonic testing applications one of three types of elastic waves are used, namely volume waves, surface waves and guided waves [7]. In this paper, guided ultrasound waves are used, as these are easy to excite by a fixed excitation source and propagate over long distances while being sensitive to internal defects in the structure [8]. These properties make guided waves particularly useful for maintenance inspections, where detecting subsurface defects in large areas is crucial. Different technologies for the contactless detection of guided ultrasound waves exist. One of the most prevalent detection technologies is laser vibrometry, where a laser beam is directed at the surface of the material and the displacement due to the ultrasound waves is measured by a distance or velocity measurement [9]. This approach is fast and enables the detection of ultrasound waves over large distances up to several meters. However, the quality of the received signal largely depends on the surface reflective properties of the tested material. Highly reflective as well as dirty surfaces like those found in a maintenance environment are often not suitable to this approach. Furthermore, most research with laser vibrometry for contactless ultrasonics is conducted in a lab environment on flat surfaces, as more complex geometries can pose challenges to the measurement process.

As an alternative, air-coupled microphones can be used for contactless detection of guided ultrasound waves. With this approach, sound pressure waves radiated from the tested material into the air are measured to detect the waves. This makes it independent of the surface's reflective properties and therefore, this approach is chosen for this work. The challenge in air-coupled detection is that radiated sound waves into the air are very weak and only detectable with specialized sensors [10]. Few studies on the measurement of guided waves using air-coupled microphones in CFRP materials exist. For instance, Wang, Allemann and Solodov et. al. have used air coupled microphones to measure guided waves in CFRP specimens and locate damages in flat material samples [11][12][13]. In a study by Armin Huber, guided waves have been used to inspect a CFRP hydrogen tank prototype using a fully air-coupled system on a robot arm [14]. The used measurement systems in these publications use ultrasound microphones of significant size with a narrow bandwidth around a center frequency in the kHz range.

In this work, the use of a laser-based optical microphone for the detection of guided waves in CFRPs positioned by a robot arm is proposed. Unlike conventional air-coupled sensors, this microphone operates without a mechanical membrane, providing high sensitivity and a significantly higher bandwidth up to frequencies in the MHz range. This allows it to capture weak ultrasonic signals in air across a broad frequency spectrum, making it particularly effective for detecting guided waves in real-world environments. Its compact size and small aperture allow the deployment using robot arms in confined or complex geometries, making it particularly well-suited for non-destructive testing in minimally invasive maintenance scenarios.

This paper explores the application of guided ultrasound waves, outlining their theory and practical implementation. Section 2 provides a theoretical background on guided ultrasound waves, introducing their propagation characteristics and significance in non-destructive evaluation. Section 3 describes the experimental setup used to investigate these waves, including instrumentation and tested materials. Section 4 presents the experimental results, demonstrating the capabilities of the proposed method. Finally, Sections 5 and 6 discuss the findings, propose directions for future research, and conclude with a summary of key insights.

2. THEORETICAL BACKGROUND OF GUIDED ULTRASOUND WAVES

Guided ultrasound waves are types of elastic waves that propagate in thin-walled structures like plates. These waves are often termed "Lamb waves" after the mathematician Sir Horace Lamb, who first described their dynamics in 1917 [15]. Due to the fact that the theoretical Lamb wave equations assume an infinitely long material, which does not exist in practice, the more general term "guided waves" is used in this paper. Figure 1 shows the three fundamental mode types in which guided waves can propagate. In the symmetric wave mode, the particle motion is symmetric with respect to the mid-plane of the plate. In this wave mode, a pressure wave travels through the plate. In the antisymmetric wave mode, the particle motion is antisymmetric with respect to the mid-plane of the plate and the wave travels through the material similar to a bending wave. In the shear-horizontal wave mode, a shear wave travels through the plate and the particle motion lies completely in the plane of the plate.

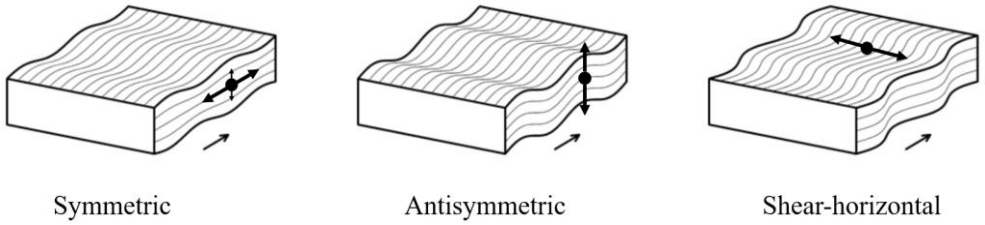

Figure 1: The three different fundamental mode types of guided ultrasound waves with their particle motion directions visualized. Adapted from [9].

Higher-order wave modes with more complex propagation patterns exist for all of the fundamental modes at higher frequencies, but they are usually harder to excite and measure and are limited in propagation range [16]. Wave modes are termed after their order, meaning S0 and A0 are the fundamental symmetric and antisymmetric wave modes, S1 and A1 are the first-order modes and so on. As the fundamental wave modes usually have the highest signal amplitude, the S0 and A0 modes are of most significance for the detection of damages using guided waves.

For the contactless air-coupled detection of ultrasound waves, the out-of-plane particle motion of each wave mode is of most significance, as it produces the strongest signals for an air-coupled transducer. This is due to the fact that in-plane particle motion does not excite significant pressure waves in the surrounding air like out-of-plane motion. Only in the antisymmetric wave mode, the particle motion is primarily in out-of-plane direction to the plate and therefore usually easiest to detect. In the symmetric wave mode, in-plane pressure waves travel through the material. Due to transverse contraction, there is a proportion of out-of-plane particle motion making this wave mode detectable, but usually with a weaker signal. Since the particle motion of the shear-horizontal mode is in-plane, and it does not cause a significant local pressure change in the material, there is minor transverse contraction and therefore only minor out-of-plane particle motion [9]. This makes the shear-horizontal mode barely detectable by contactless means and it is therefore neglected in this work.

Guided ultrasound waves have dispersive behavior, meaning the wavelength and velocity depend on the frequency and plate thickness. A dispersion diagram showing the relationship between wavenumber, representing the number of waves per meter, and frequency is depicted in Figure 2 (left).

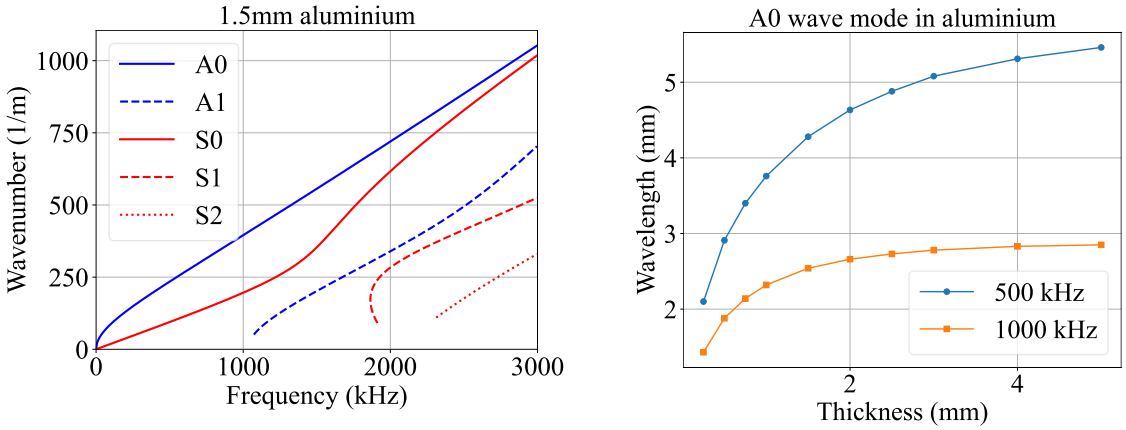

Figure 2: Dispersion diagram of guided waves in a 1.5 mm thick aluminium plate (left) and diagram showing the wavelength-thickness relationship at two frequencies (right). Calculated using the dispersion calculator (DC) tool [17]

In a dispersion free wave, the phase velocity is independent of the frequency. The relationship between wavenumber and frequency would therefore be represented by a line in the wavenumber-frequency plot that crosses the origin. As seen in Figure 2 (left), guided waves have a nonlinear relationship between wavenumber and frequency and this relationship differs for different wave modes.

The wavelength of guided waves of is usually larger than the thickness of the material they propagate in. Figure 2 (right) depicts the wavelength of the A0 wave mode in aluminium for different thicknesses and frequencies simulated using the dispersion calculator (DC) tool [17]. According to the simulations, the wavelength of the A0 mode is always the lowest at all frequencies of all wave modes. This can be deducted from Figure 2 (left), as it has the highest wavenumber at all frequencies and the wavelength is the inverse of the wavenumber. As seen in Figure 2 (right), with thicker materials, the wavelength of the guided waves increases. At higher frequencies, the wavelength decreases. For many approaches, damages in the material should be at the order of, or larger than the wavelength of the used ultrasound waves. Visualizing defects with guided ultrasound waves is therefore mostly suitable to thin materials up to a few millimeters thickness and larger defects on the order of a few millimeters or centimeters. To improve the resolution, higher frequencies can be utilized that have lower wavelengths. Also, nonlinear approaches for data processing exist that have been able to detect defects that are much smaller than the wavelength, down to a few micrometers [18]. The properties of guided ultrasound waves can be used in various testing methods to find defects in materials. For instance, thickness variations in materials can be found by a change in wavelength of the guided ultrasound waves, and this effect can be used to locate internal delaminations in composite materials [18].

3. EXPERIMENTAL SETUP

The experimental setup consists of a robot arm (UR-10) on a lab table where the tested material is positioned as depicted in Figure 3. The guided ultrasound waves are excited by a cylindrical monolithic piezoelectric ceramic (diameter 10 mm, thickness 0.25 mm or 0.5 mm, material PIC255, manufacturer: PI) glued to the surface of the tested material. The piezoelectric transducers are excited by a rectangle voltage pulse using a USB-ultrasound device (PCUS single pro). The optical microphone (Xarion ETA450 T-Shape) is attached to the robot end effector with a custom mount. For all measurements, the low-frequency cutoff of the microphone was set to 100 kHz and the gain to 0 dB. The microphone puts out an electric signal that is measured by an oscilloscope (PicoScope 4842A). The robot control and data processing is handled by a personal computer running a custom Python script saving the experimental data in HDF5 format.

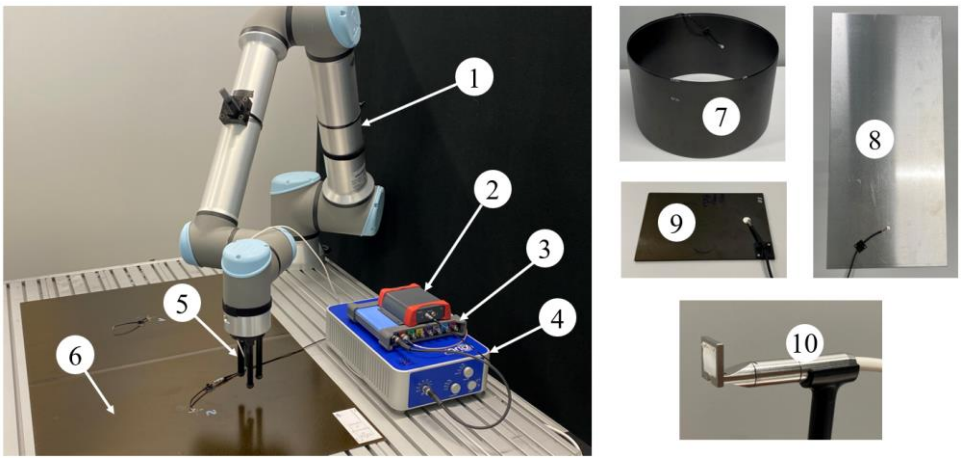

Figure 3: Experimental setup for the automated imaging of wavefield data. (1) Robot; (2) Pulse generator; (3) Oscilloscope; (4) Signal conditioning unit; (5) Microphone mount; (6…9) Test materials; (10) Microphone

For the measurements, the following material samples have been used: CFRP plate made from Hexcel M21/IMA-12K material with $[-45°, 0°, 45°, 90°]_s$ layup at 1.05 mm thickness (6); A CFRP cylinder segment with 350 mm diameter made of Teijin Q183 material with 2.5 mm thickness with $[90°_4,0°_2]_s$ layup (7); a 1.5 mm thick aluminium plate (8); And a CFRP coupon with 3.3 mm thickness made of Hexcel M21 (9). To acquire a wavefield image, the robot arm moves to different positions with the same orthogonal distance to the test material in a grid pattern. For each position, an ultrasound pulse is generated by the excitation unit and the response is measured by the optical microphone. A trigger signal synchronizes the measurement and excitation in time. By repeating this process, the wavefield in a specified area can be measured.

4. EXPERIMENTAL RESULTS

With the previously described measurement setup, a time-series measurement can be taken at different positions above the tested material. A typical signal at one of the measurement positions captured from a carbon fiber composite plate is depicted in Figure 4. The signal is measured in the 1.05 mm thick CFRP plate about 14 cm away from the excitation source and a 500 ns rectangle pulse is used for excitation.

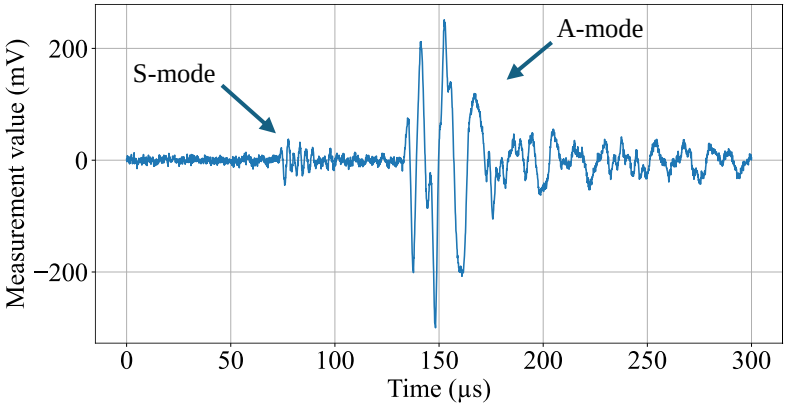

Figure 4: A typical time domain signal of a guided ultrasound wave in CFRP. The signal shows a faster wave mode arriving first and a slower wave mode arriving second.

In Figure 4, earlier than approximately 75 µs after the excitation, the signal is zero and only noise is present. After a certain time, depending on the distance of the microphone from the excitation source, a signal with relatively low amplitude and high frequency is usually detected. A numerical simulation using the DC tool shows that the energy velocity of the fundamental symmetric wave mode is the highest at the dominant frequencies. Therefore, the wave arriving at approximately 75 µs in Figure 4 is assumed to be the fundamental symmetric wave mode. Later, at approximately 130 µs in Figure 4, a stronger signal with lower dominant frequency arrives. This signal is likely representing the antisymmetric wave mode, as it is expected to cause stronger signals as described in Section 2.

To validate that the test setup is able to accurately detect the expected behavior of the guided waves in tested materials, a dispersion diagram is measured by sampling 600 points at 0.5 mm spacing along a line that is oriented in the main wave propagation direction. In order to reduce uncertainties in the material properties of the carbon fiber samples, the measurement is taken with a 1.5 mm thick aluminium plate. To excite high frequencies, a short 100 ns rectangle pulse is used. A dispersion diagram is obtained by applying a two-dimensional Fourier transform to the space-time measurement matrix, resulting in a wavenumber-frequency plot as depicted in Figure 5. The measurement values are normalized and shown in logarithmic color scale to highlight weak signals. The dispersion relation is simulated using the DC tool and overlaid on the measurement data. The result shows a good match between the simulated wavenumber-frequency curve and the measured values, indicating that the test setup is able to accurately image the wavefield. As seen in Figure 5, The different wave modes A0, A1, S0, S2 and traces of S1 are detected. The dispersion diagram demonstrates the very high bandwidth of the used optical microphone, as the measured dispersion curves span from 50kHz up to almost 3 MHz. For low frequencies, the matching between measurement and simulation is close, for higher frequencies the wavenumber tends to be higher in the simulation than in the measurement. This could be caused by an uncertainty in the material parameters, as the exact alloy of the used specimen is not known. Also, it could be a result of a non-ideal alignment of the measurement direction with the wave direction.

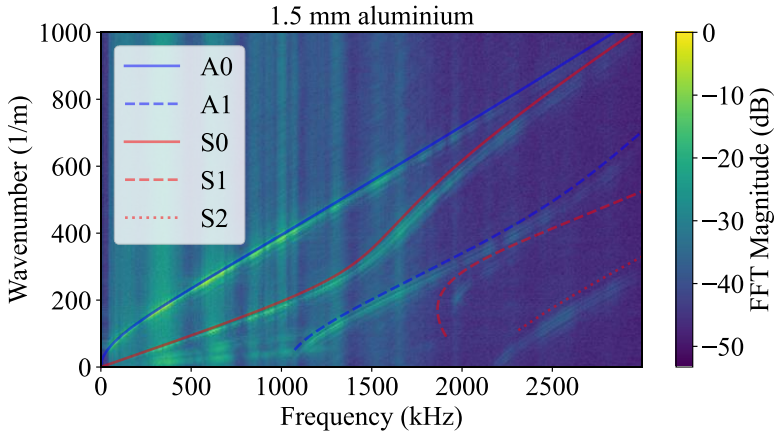

Figure 5: Comparison of a simulated dispersion relation in 1.5 mm thick aluminium with measured values. The simulation and measurement match, demonstrating that the experimental setup delivers valid results.

The measurement shows varying intensities for different frequencies in a pattern, as visible by vertical lines in Figure 5. For higher frequencies, the intensity is generally lower compared to low frequencies. The uneven distribution of frequency components could be a result of the specific frequency response of the piezoelectric transducer with different resonant frequencies and their higher harmonics. In future work, this could be further investigated to optimize the excitation.

By repeating the experiment for many points in a grid above the surface of the tested material, the measurements can be combined into a matrix representing the signal amplitude over space and time. By plotting the signal value at a fixed time for each position, a wavefield image can be obtained. In Figure 6, a wavefield measurement with a grid of 200 by 200 points and a grid spacing of 0.5 mm imaging the area around the excitation is shown. The measurement was performed on the 1.05 mm thick CFRP plate mentioned in Section 3.

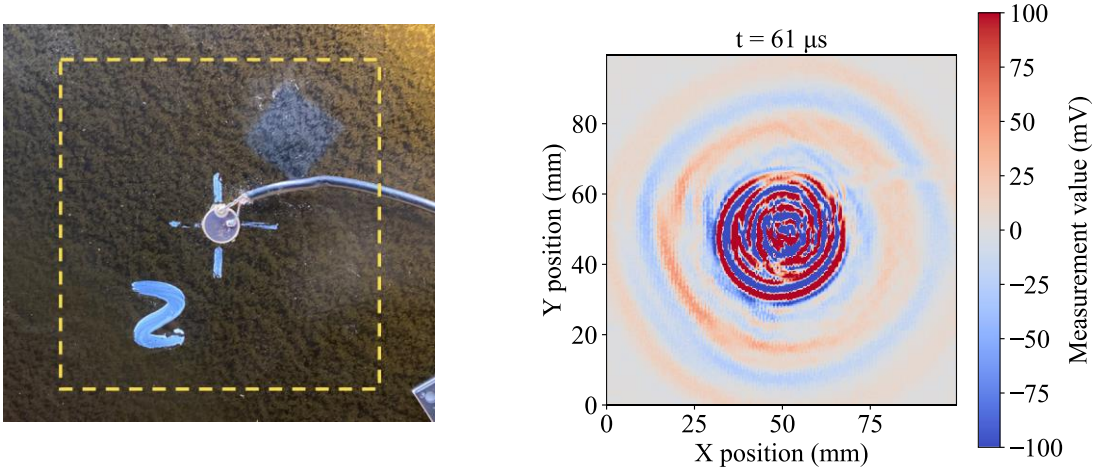

Figure 6: Picture of scanned region on CFRP plate with piezoelectric excitation and corresponding wavefield image showing the propagation of different wave modes.

In the resulting wavefield image, two wavefronts propagating in all directions away from the excitation source are visible. One wavefront with a long wavelength further away from the center and a wavefront with lower wavelength and significantly stronger signal closer to the center can be observed. The time point at 61µs is relatively soon after the excitation, as the waves have not yet traveled beyond the imaged area. This is evident in the corners of the plot where very low values are displayed, corresponding to the measurement noise. The cable used to contact the piezoelectric actuator is also visible as an artefact at the right side of the wavefield image. The measurement shows a high spatial resolution of 0.5 mm grid spacing with a sufficient amount sampling points per wavelength to represent the low-wavelength antisymmetric wave mode. Therefore, this measurement shows that the described setup can achieve a sufficient spatial

sampling density to acquire high-detail wavefield images. Further measurements showed that even higher resolutions down to 0.1 mm grid spacing are possible, but not necessary to accurately image the wavefield. As seen in Figure 6, the wavefronts are not exactly circular and the wave propagation pattern shows some irregularities. This becomes particularly apparent in the faster wave mode traveling in negative y-direction as well as in the center where the slower wave mode shows deviations from the ideal circular pattern. These deviations likely arise due to the anisotropic properties of the tested material and inhomogeneities in the radiation pattern of the excitation.

To test the ability to detect damages in the material, a dent in the surface of the CFRP plate with about 5 mm length and 2 mm width is scanned. Figure 7 shows the imaged area and resulting wavefield image changed by the defect.

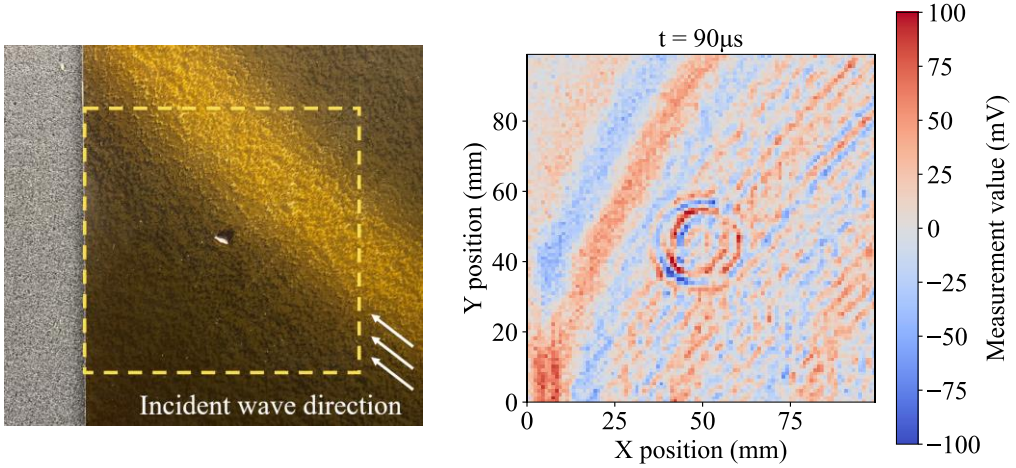

Figure 7: Wavefield image around damage asymmetric to the thickness of the plate. The incident wave travels in upper left direction.

At the time point of the depicted wavefield image of 90 µs, the wavefront of the faster wave mode just passed over the defect and the slower mode has not yet reached the imaging area. From the resulting wavefield image, it is visible that the defect generates a circular wave propagating away from the defect location. This likely represents a mode conversion of the incident symmetric wave mode into the antisymmetric mode as described in [20]. As the signal of the antisymmetric wave mode is usually stronger than that of the symmetric mode as described in section 2, the mode converted wave shows a contrast to the incident wavefield even though only a small portion of the incident wave`s energy is converted. By choosing a suitable time for the wavefield image, the defect location is highlighted by the mode converted wave as seen in Figure 7. Using this approach, a variety of defects like dents and scratches can be detected and by further signal processing, the mode converted waves could be filtered out. This effect, however, only occurs for defects that are non-symmetric to the mid-plane of the plate as described in [20].

A different type of damage commonly found in composite materials are internal delaminations, which can be caused by impact damages. If delaminations are caused by an impact, the impact location is sometimes visible as a small dent on the surface of the material, depending on the impulse energy and impactor shape. The underlying internal delamination, however, is often significantly larger than the dent caused by the impact. As delaminations lie in-between the material layers, they do not act as non-symmetric damage with respect to the mid-plane as described before and therefore do not lead to mode conversion as described in [20]. To test the ability to detect delaminations, a CFRP plate is imaged that has previously been impacted for a study by Jacob et. al, where the testing results of ultrasonic and thermography scans for detecting delaminations are compared [19]. The material has been impacted by a mobile impact cannon with a hemispherical head with a diameter of 16 mm with an impact energy of 13.7 J. A piezoelectric ceramic with 0.5 mm thickness is glued to the material for wave excitation. The resulting wavefield is shown in Figure 8.

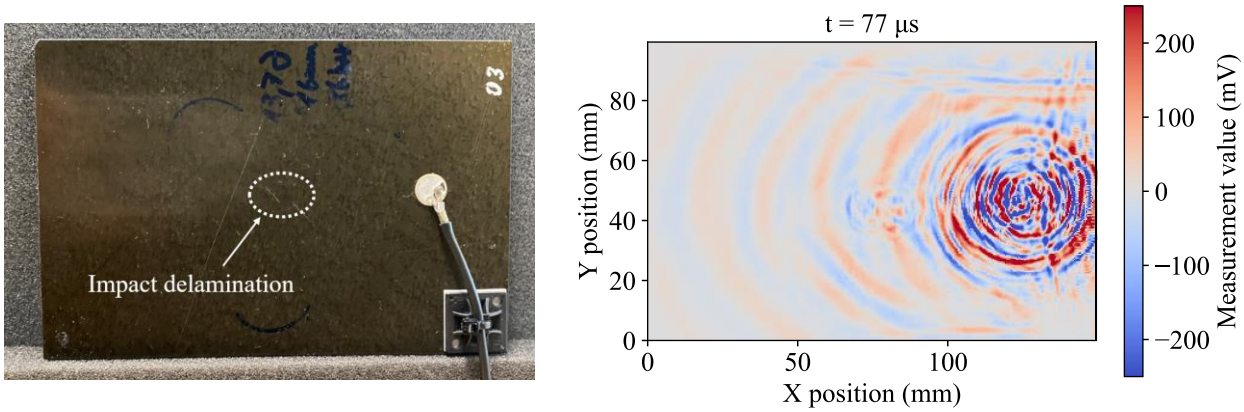

Figure 8: Impacted CFRP coupon with marked delamination location and corresponding wavefield with a visible alteration in the middle.

In the resulting wavefield, the excitation is visible at the right side of the plate, as the origin of the guided waves. Again, the faster wave modes are visible with higher wavelength and lower intensity, as well as the slower wave modes with higher intensity and lower wave speed. The delamination is located at the center of the plate and an alternation of the wave pattern is evident at its location. This result shows that the measurement setup is able to detect internal damages in CFRP materials that are not visible from the outside.

As seen in Figure 8, defect-related waves are often overshadowed by higher amplitude incident waves or their reflections at the sample's edges. Different methods for highlighting or extracting defect information exist, but most of them have been tested on data acquired using laser vibrometers [18]. One of these methods is Ultrasonic Frequency Tomography, where the wavefield is decomposed into frequencies using a Fourier transform along the time axis of each individual signal. However, this process results in the loss of the time dimension. In Wavelet-transformed Ultrasonic Propagation Imaging (WUPI) as proposed by [22], a wavelet decomposition is used so that the wavefield data can be sliced along the time and frequency axes, preserving both dimensions. For this analysis, a "cmor1.5-1.0" wavelet has been used for the decomposition and the wavefield data of Figure 8 is analyzed. By plotting the wavelet coefficients in a heatmap, the amplitude of specific frequencies at a given time can be visualized. In Figure 9, at 239 kHz and 107.6 µs, the magnitude of all non-defect-related signals is significantly reduced. The location of the delamination is clearly visible and also the rough size can be estimated. Using this method, the highlighted area roughly aligns with water-contacted ultrasound C-scans of the delamination in shape and location.

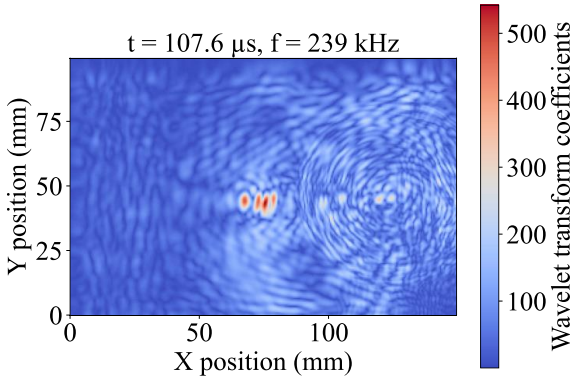

Figure 9: Wavelet transformed image of the wavefield visualizing the defect location and approximate size.

By storing the data in a format optimized for quick access, the five-dimensional data can be interactively sliced by frequency and time. This allows for efficient switching between different time-frequency pairs and eliminates the need to identify useful frequencies in advance, as proposed by [22].

To demonstrate the flexibility of the setup using a robot arm equipped with the optical microphone, a wavefield measurement of the carbon fiber composite tube segment described in section 3 is taken as seen in Figure 10. As the texture of the outside surface of the tube segment is very rough, the piezoelectric ceramic is glued to the inner wall of the tube which is smoother. To image the wavefield, the robot moves in a grid, curved in a semi-circle around the center axis of the tube. The measurement is taken at the outside of the tube with a constant distance to the surface.

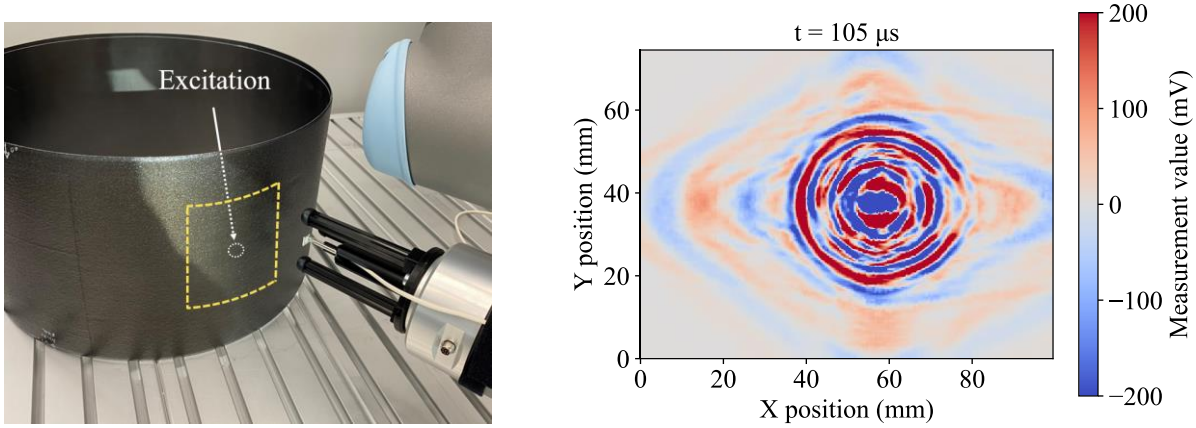

Figure 10: Picture of CFRP cylinder with marked imaging area and corresponding wavefield measurement

As seen in Figure 10, the measurement approach enables imaging of the wavefield also with the curved surface of the tube segment. This demonstrates that the measurement approach is applicable to more complex geometries like those that can be found aircraft maintenance. As the CFRP tube segment consists only of 0° and 90° layers, it is not quasi-isotropic like the specimens in Figure 6,Figure 7 and Figure 8. This anisotropy is also evident in the wavefield image as the wavefront of the faster wave mode visible in Figure 10 is deformed to a V-shape in the x and y directions. This could be resulting from the wave speed in the fibers being higher than the wave speed in the matrix of the material.

5. DISCUSSION AND FUTURE WORK

The experimental results seen in section 4 show that the approach of using an optical microphone with a robot arm to image the guided ultrasound wavefield in CFRP works. Furthermore, analysis of the data enables localizing and sizing of internal defects in CFRP materials. For a practical application of the technology in a maintenance environment, however, multiple challenges exist. One challenge is the time needed to perform the measurements. For high-resolution wavefield images like those shown in Figure 6, Figure 7, Figure 8 and Figure 10, several ten thousand points have to be sampled. When the robot arm stops at each point to take a measurement, as done for the experiments in this paper, this amounts to measurement times above one hour for small 10 cm by 10 cm images with a measurement repetition rate below 5 measurements per second. To increase the sampling speed significantly, the robot could move continuously with the measurements triggered dynamically. However, even with this approach, there is an upper limit to the sampling speed. As a pulse is generated for each measurement point, the waves generated by the previous pulse could interfere with the current one for high repetition rates. An efficient system could therefore combine methods that work with sparse sampling to find the rough locations of damages and use high-resolution imaging only in relevant areas to characterize defects.

The described approach offers a contact-free detection of guided ultrasound waves. In contrast to classical ultrasound technology, a single contacted transducer enables high-resolution imaging of a large area. For use cases where contacting a transducer is not applicable, different excitation methods like air-coupled transducers, electromagnetic acoustic transducers (EMATs) or laser excitation could be explored. If this approach is to be used in combination with a guided wave structural health monitoring (SHM) system, the transducers embedded in the structure could be used as excitation sources. Using a six-degree-of-freedom robot arm to move the optical microphone to different positions above the material is a novel approach for imaging guided waves, that has not been extensively studied in literature up to this point. The advantage of this setup lies in the very high degree of flexibility with regard to the geometry of the tested material, making the approach suitable to real-world components. However, using a robot arm comes with its own challenges. For accurate

wavefield images, precise positioning of the microphone is of high importance. In additional tests it became evident that artifacts in the resulting wavefield image arise, when the robot approaches positions in neighboring rows from different directions, as often done to save time by scanning rows in alternating directions. Future studies could be performed to quantify the effect of robot inaccuracies with respect to the resulting wavefield image in different areas of the workspace and configurations. In this study, test materials have been used for the experiments. In future work, tests on maintenance-relevant aircraft components could be performed to assess the suitability of the approach for a practical application on specific components. As the optical microphone is very small compared to traditional air-coupled ultrasound transducers, it could be used in space-sensitive applications, like inspections near tight corners or in enclosed spaces like those found inside an airplane. With this flexibility, components could be scanned without the need for removal, enabling on-wing minimally-invasive testing.

6. CONCLUSION

In this paper, a laser-based optical microphone is used in combination with a six-degree of freedom robot arm to detect and visualize guided ultrasound waves in different carbon fiber reinforced composite samples. It is shown that this approach accurately images the expected wavefield as demonstrated by comparing a measured dispersion diagram in aluminium to a simulated one. Multiple wavefield images of carbon fiber composite materials are shown, visualizing different wave modes traveling through the material. The detectability of two different types of damage is demonstrated by the visualization of a single-sided dent and an internal delamination. By applying a wavelet-based wavefield analysis, it is shown that the delamination can be highlighted and the location and approximate size can be estimated. The scalability of the used testing approach to more complex structures is demonstrated by a measurement on a composite tube segment and potentials as well as limitations are discussed.

ACKNOWLEDGEMENTS

would like to thank the DLR Institute for lightweight systems in Stade, germany for providing the CFRP cylinder segment used in this work.

REFERENCES

[1] Zhang, J., Lin, G., Vaidya, U., & Wang, H. (2023). Past, present and future prospective of global carbon fibre composite developments and applications. *Composites Part B: Engineering*, *250*. https://doi.org/10.1016/j.compositesb.2022.110463

[2] Timmis, A. J., Hodzic, A., Koh, L., Bonner, M., Soutis, C., Schäfer, A. W., & Dray, L. (2015). Environmental impact assessment of aviation emission reduction through the implementation of composite materials. *International Journal of Life Cycle Assessment*, *20*(2), 233–243. https://doi.org/10.1007/s11367-014-0824-0

[3] Luo, Z., Wang, H., Huang, Y., Shen, P., Zheng, E., & Zhang, H. (2024). Nondestructive detection of CFRP subsurface defects using transient lock-in thermography. *Journal of Thermal Analysis and Calorimetry*. https://doi.org/10.1007/s10973-024-13130-7

[4] Helfen, T. B., Venkat, R. S., Rabe, U., Hirsekorn, S., & Boller, C. (2012). Characterisation of CFRP through enhanced ultrasonic testing methods. *Applied Composite Materials*, *19*(6), 913–919. https://doi.org/10.1007/s10443-012-9250-2

[5] Cheng, L., & Tian, G. Y. (2012). Comparison of nondestructive testing methods on detection of delaminations in composites. *Journal of Sensors*, *2012*. https://doi.org/10.1155/2012/408437

[6] Song, P., Liu, J., Li, Z., Wu, S., Sun, X., Yue, H., & Pawlak, M. (2022). All-optical laser ultrasonic technique for imaging of subsurface defects in carbon fiber reinforced polymer (CFRP) using an optical microphone. *Journal of Applied Physics*, *131*(16). https://doi.org/10.1063/5.0087304

[7] Nsengiyumva, W., Zhong, S., Lin, J., Zhang, Q., Zhong, J., & Huang, Y. (2021). Advances, limitations and prospects of nondestructive testing and evaluation of thick composites and sandwich structures: A state-of-the-art review. In *Composite Structures* (Vol. 256). Elsevier Ltd. https://doi.org/10.1016/j.compstruct.2020.112951
[8] Ma, Z., & Yu, L. (2019). Lamb wave defect detection and evaluation using a fully non-contact laser system. https://doi.org/10.1117/12.2514048
[9] Raddatz, F. (2016). Lokalisierung der Interaktionsorte von Lambwellen in komplexen Faserverbundstrukturen. PhD thesis, Institut für Faserverbundleichtbau und Adaptronik.
[10] Chimenti, D. E. (2014). Review of air-coupled ultrasonic materials characterization. *Ultrasonics*, *54*(7), 1804–1816. https://doi.org/10.1016/j.ultras.2014.02.006
[11] Wang, B., Shi, W., Zhao, B., Tian, X., & Tan, J. (2024). Detecting delamination defects in CFRP plates using nonlinear defect index of air-coupled Lamb waves and adaptively weighted imaging algorithm. *Mechanical Systems and Signal Processing*, *208*. https://doi.org/10.1016/j.ymssp.2023.111023
[12] Alleman, G., Pelt, M. M. J. M., & Groves, R. M. (2014). Air-coupled ultrasound for damage detection in CFRP using Lamb waves and ultrasonic verification.
[13] Solodov, I., Döring, D., & Busse, G. (2010). Air-Coupled Lamb and Rayleigh Waves for Remote NDE of Defects and Material Elastic Properties. In *Strojniški vestnik-Journal of Mechanical Engineering* (Vol. 56).
[14] Huber, A. (2023). Air-coupled Ultrasonic Inspection of Thermoplastic Composite Structures for Aerospace Vehicles. *Research and Review Journal of Nondestructive Testing*, *1*(1). https://doi.org/10.58286/28105
[15] Lamb, H.: On Waves in an Elastic Plate. Proceedings of the Royal Society of London A, pages 114–128, 1917
[16] Kazys, R. J., Sestoke, J., & Mazeika, L. (2022). Excitation and Reception of Higher-Order Guided Lamb Wave's A1 and S1 Modes in Plastic and Composite Materials. *Materials*, *15*(20). https://doi.org/10.3390/ma15207249
[17] A. Huber, "Dispersion Calculator (DC), available at." https://github.com/ArminHuber/Dispersion-Calculator.
[18] Zheng, S., Luo, Y., Xu, C., & Xu, G. (2023). A Review of Laser Ultrasonic Lamb Wave Damage Detection Methods for Thin-Walled Structures. In *Sensors* (Vol. 23, Issue 6). MDPI. https://doi.org/10.3390/s23063183
[19] Jacob, G., Tuppatsch, J., Schmidt, D., Pototzky, A., Rodeck, R., Raddatz, F., & Wende, G. (2024). *NON-DESTRUCTIVE TESTING OF CHALLENGING AEROSPACE STRUCTURES*. https://doi.org/10.25967/630245
[20] Willberg, C., Mook, G., Gabbert, U., & Pohl, J. (2014). *Lamb wave mode conversion in CFRP plates*. https://doi.org/10.13140/2.1.3372.4161
[21] Xie, L., Lian, Y., Du, F., Wang, Y., & Lu, Z. (2024). Optical methods of laser ultrasonic testing technology in the industrial and engineering applications: A review. In *Optics and Laser Technology* (Vol. 176). Elsevier Ltd. https://doi.org/10.1016/j.optlastec.2024.110876
[22] Lee, J. R., Ciang Chia, C., Jin Shin, H., Park, C. Y., & Jin Yoon, D. (2011). Laser ultrasonic propagation imaging method in the frequency domain based on wavelet transformation. *Optics and Lasers in Engineering*, *49*(1), 167–175. https://doi.org/10.1016/j.optlaseng.2010.07.008